

Article

A 2-DOF Impact Actuator for Haptic Application

Sangyoon Kim ¹, Woochan Lee ^{2,*} and Jaeyoung Park ^{3,*}

¹ Department of Mechanical and Aerospace Engineering, Seoul National University, Seoul 08826, Korea; oiei0806@snu.ac.kr

² Department of Electrical Engineering, Incheon National University, Incheon 22012, Korea

³ Department of Computer Engineering, Hongik University, Seoul 04066, Korea

* Correspondence: wlee@inu.ac.kr (W.L.); jypdeca@hongik.ac.kr (J.P.)

Abstract: The demand for realistic haptic feedback actuators has increased as mobile devices have increased in popularity. However, most current haptic actuators provide limited 1-DOF tactile sensations, such as vibrations. This paper presents a 2-DOF haptic impact actuator that can provide planar directional (e.g., x and y directional) and magnitude tactile cues to a user. We built an impact actuator that was designed to be of such a size that a user can grasp it with one hand. Multiple electromagnets of the actuator drive a permanent magnet to hit the actuator housing, creating an impact. For the control of the impact direction, we assumed the direction of a magnetic field vector at the centre of the actuator would follow that of a reference vector formed by voltage heading into the electromagnet array. The results of magnetic field measurements support our assumption by showing that the trend of the magnetic field vector coincided with that of the reference voltage vector. Furthermore, the measurement of the impact acceleration showed the trend that the impact direction follows the reference voltage vector.

Keywords: haptics; impact actuator; magnetic field; 2-DOF; electromagnets



Citation: Kim, S.; Lee, W.; Park, J. A 2-DOF Impact Actuator for Haptic Application. *Actuators* **2022**, *11*, 70. <https://doi.org/10.3390/act11030070>

Academic Editor: Kenji Uchino

Received: 12 January 2022

Accepted: 23 February 2022

Published: 24 February 2022

Publisher's Note: MDPI stays neutral with regard to jurisdictional claims in published maps and institutional affiliations.



Copyright: © 2022 by the authors. Licensee MDPI, Basel, Switzerland. This article is an open access article distributed under the terms and conditions of the Creative Commons Attribution (CC BY) license (<https://creativecommons.org/licenses/by/4.0/>).

1. Introduction

Since the introduction of smart devices, there have been constant demands to provide a more effective user experience. To meet their needs, manufacturers and researchers have paid attention to the potential of haptic feedback technologies that can create the sensation of touch. Most actuators that have been used for smart applications are vibrotactile actuators, including ERM motors, LRAs, and piezo-actuators. While they have distinct mechanical characteristics, their common feature is providing 1-DOF haptic feedback. Since a human can sense tactile sensations in a wide range of frequencies, even a 1-DOF haptic actuator can produce a variety of tactile effects, such as pushing a button and providing vibrations to signal an incoming call. However, a 1-DOF actuator cannot emulate the sensation of localized contact, such as contact in a specific direction, within a smart device or a controller for virtual applications. This issue led us to come up with a 2-DOF haptic impact actuator driven by multiple electromagnets.

Both industries and academia have developed various haptic impact actuators to emulate crisp tactile sensations, such as key-click. For example, the piezo actuator was spotlighted due to its fast response time and ability to generate vibrotactile signals similar to those it imitated [1]. However, more common haptic actuators for mobile devices are driven by magnetic force, including LRAs and Apple's Taptic engine. Such a haptic actuator is typically a spring-mass system where an electromagnet drives the mass and creates a strong haptic impact due to high energy density [2,3]. Most of the magnetic force-driven haptic actuators have rather simple structures for the sake of compact size, which constrains them to have only a single degree of freedom for haptic impact. Due to the design complexity, few studies have proposed multi-DOF haptic impact actuators based on magnetic force [4–6].

Most multi-DOF haptic actuators have been developed to provide contact force vector information or localized tactile patterns. The multi-DOF haptic actuators providing contact vector information are designed to supplement a force-feedback interface that can render kinesthetic sensation [7–10]. Such actuators typically have complex mechanical linkage structures to move the contact element, which results in heavy and large actuators. To provide localized tactile patterns, researchers have developed various types of actuators, such as pin-arrays [11–13] and electrotactile actuators [14]. Such an actuator typically consists of multiple sub-actuators to stimulate a user's local skin. The aforementioned haptic actuators can successfully provide localized tactile patterns. However, most of them fail to provide a salient haptic sensation due to the limitations of their working mechanisms, such as small stroke, small travel length or slow speed [15,16]. Multiple studies have come up with solutions to resolve the issues while providing multi-DOF tactile sensations and keeping the end-effector light. One of the solutions is using the DEA, which has the characteristic of deforming its surface when a high voltage is applied. Using the property, researchers have developed light haptic interfaces with fast reaction times [17–22]. Another solution is a pneumatic haptic actuator that uses air pressure to stimulate the end-effector of a haptic interface [23–31]. The pneumatic haptic actuator has various advantages, including a light end-effector, a fast reaction time, high-intensity tactile sensations, and possibly multi-DOF feedback, depending on the functionalities of the air compressor. A common feature of pneumatic actuators and DEAs for haptic applications is the need for a large component, i.e., the air compressor or the high voltage (normally multi kV) power supply. They are typically large in weight and volume, which can be a challenge for hand-held applications that cannot allow separate power sources, such as controllers and mobile devices.

This study presents a 2-DOF impact actuator system that creates a haptic impact conveying planar (e.g., x or y directional) vector information for the haptic application. Other multi-DOF haptic actuators have impact and size issues due to their driving mechanisms. While 1-DOF actuators can create various haptic sensations, including vibrations and haptic impacts, they have limitations in creating directional cues, i.e., multi-DOF haptic impacts. More modern haptic actuators, such as pneumatic actuators and DEAs, have overcome these issues. However, they have a common flaw in taking up substantial space, due to the air compressor for a pneumatic actuator and a high voltage power supply for a DEA. This is a drawback for haptic applications requiring portability, such as a hand-held controllers and mobile applications. Noting the issues, we proposed a haptic actuator mechanism that can create a directional haptic impact by driving a permanent magnet with an array of electromagnets in our previous study [6]. The actuator could change a haptic impact's planar direction and magnitude by creating an attractive force with a local electromagnet toward the permanent magnet. Furthermore, it has a driving mechanism, i.e., an electromagnet array, inside the actuator, which does not require an outer high energy source. However, the previous study only presented the actuator prototype and did not propose any specific method to control the direction of the haptic impact. Thus, this paper presents a 2-DOF control method based on the experimental measurements. There are studies proposing analytical expressions for a magnetic force between magnets that are separated by a relatively small distance. However, our actuator consists of multiple electromagnets, which makes it highly complex to calculate the magnetic force inside the actuator [32–35]. This led us to propose a method to control the magnitude and direction of the haptic impact based on the magnetic field distribution inside the impact actuator. To prove the validity of our approach, we measured the magnetic field vector and the impact acceleration by varying the voltage supplied to the electromagnets.

Therefore, the contributions of this paper are (1) to propose a 2-DOF haptic impact actuator mechanism, (2) to present the results of magnetic field measurements and haptic impact acceleration, and (3) to evaluate the control method for our haptic impact actuator based on the experimental measurements.

2. Materials and Methods

2.1. Design of a 2-DOF Haptic Impact Actuator

We designed a 2-DOF haptic impact actuator that can control the horizontal direction and the magnitude of an impact. The actuator is cylindrical in shape. It is 30 mm high and 45 mm in diameter, which is the size that an average user can grasp with one hand. The actuator consists of three parts: (a) the upper central electromagnet part, (b) the impact magnet part, and (c) the direction-controlling electromagnet array part, as shown in Figure 1. The direction-controlling electromagnet creates the magnetic field to drive the magnet to the desired position. The wires for the electromagnets facing each other are wound in opposite directions to exert magnet forces with different polarities. The central electromagnet creates an additional magnetic field in all horizontal directions, which accelerates the outward motion of the permanent magnet. Thus, the impact magnitude is increased compared to not using a central solenoid. The upper central electromagnet is wound 4000 times around a ferromagnetic core having the inductive reactance of 45Ω . It can create a magnetic field in all horizontal directions. The impact magnet part is a void cylinder with a permanent magnet inside it. The direction-controlling electromagnet array consists of four directional electromagnet units, each of which is wound 1500 times and has inductive reactance of 13Ω .

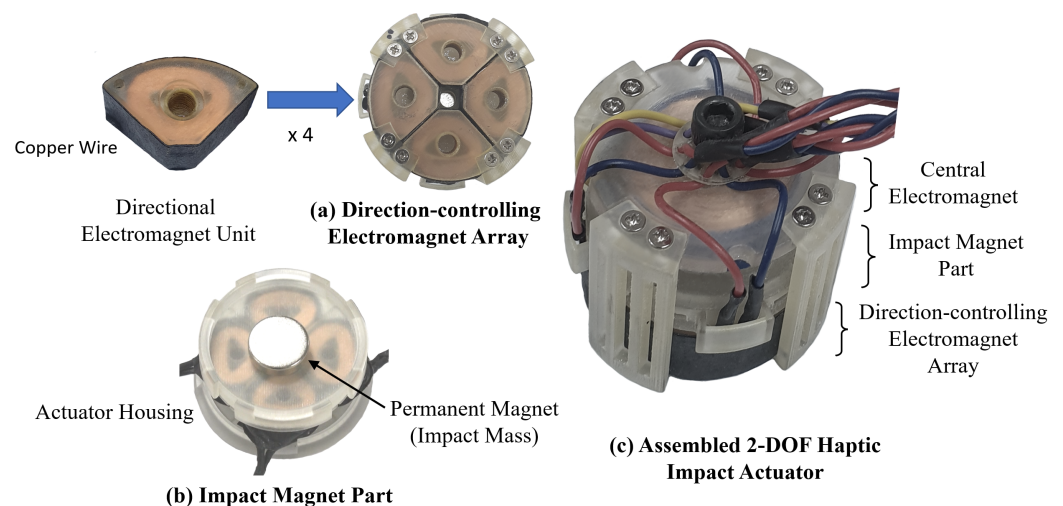


Figure 1. The components and assembly of the 2-DOF haptic impact actuator. (a) Direction-controlling electromagnet consisting of four directional electromagnet units. (b) Impact magnet unit where a permanent magnet creates an impact. (c) The assembly of the 2-DOF haptic impact actuator consisting of three parts.

The 2-DOF haptic impact actuator works in three stages, (a) neutral stage, (b) impact actuation, and (c) return stage, as shown in Figure 2. In the neutral stage, the electric current does not flow to any of the electromagnets. Then, the magnet is constrained at the central position, being attracted by the ferromagnetic force. Thus, the actuator is robust to an external shock in the neutral stage. The impact actuation stage is the stage from accelerating the magnet toward the inner wall until the impact. First, the electric current flows in a pair of directional electromagnet units to create the attractive force for the permanent magnet. Meanwhile, the central electromagnet creates a magnetic field with a repulsive magnetic force to move the permanent magnet outward. Then, the permanent magnet moves outward until it hits the inner wall of the housing. Finally, in the return stage, the electric current is turned off, and the permanent magnet moves back to the central position, being attracted by the ferromagnetic core.

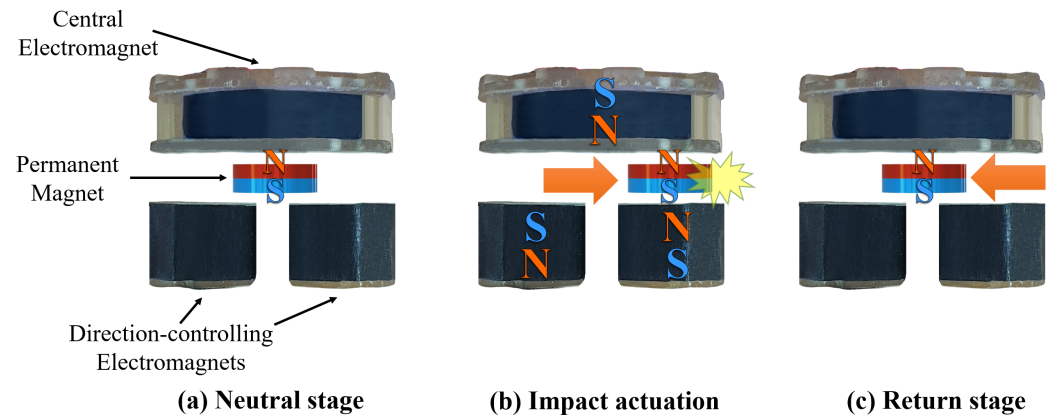


Figure 2. Three working stages of the 2-DOF haptic impact actuator.

We used Solidworks (Dassault Systems Solidworks Corp., Waltham, MA, USA) software to design the actuator housing. The actuator housing prototype was fabricated with transparent resin (VisiJet M3 Crystal, 3D Systems Inc., Rock Hill, SC, USA) by a 3D printer (ProJet HD3500, 3D systems, Rock Hill, SC, SA). For each electromagnet, we wound copper wire around the housing by using a geared motor with an encoder (GM36A-3229E, Motorbank, Korea).

2.2. Control of a Magnetic Field from Multiple Sources for a 2-DOF Impact

For the control of a 2-DOF haptic impact, the magnitude of the impact needs to be controllable. Since the impact I is $m\Delta v$, the impact magnitude can be controlled by adjusting the initial magnetic force applied to the permanent magnet. Furthermore, the direction of the impact can be controlled by adjusting the direction of the initial magnetic force applied to the permanent magnet. To estimate the force, we first assume that the permanent magnet is an electromagnet, based on the work of Ravaut et al. [33]. In that case, the magnetic force between two electromagnets a and b , F_{ab} separated by the distance d_{ab} , is expressed as

$$F_m = a_{ab} N_a N_b \frac{\mu_0 I_a I_b}{2\pi d_{ab}}, \quad (1)$$

where a_{ab} , μ_0 , N_a , N_b , I_a , and I_b are a unit vector connecting a and b , the permeability, a 's number of windings, b 's number of windings, the current flowing in a , and the current flowing in b , respectively [36]. Let us assume that there are K sources for the magnetic field, and denote the horizontal position of each source as p_i , considering that the permanent magnet is constrained on a plane. Then, the horizontal component of the magnetic field vector at a point p_x can be expressed as

$$B_x = \sum_{i=0}^{K-1} a_{ix} N_i \frac{\mu_0 I_i}{2\pi d_{ix}} = \frac{\mu_0}{2\pi} \sum_{i=0}^{K-1} a_{ix} \frac{N_i I_i}{d_{ix}}, \quad (2)$$

where a_{ix} , I_i , and d_{ix} denote a unit vector connecting p_i and p_x , the current of the i -th source, and the distance between p_i and p_x . Then, the direction of the magnetic field vector B_x can be estimated from the vector sum of $N_i I_i a_{ix}$. Each vector component $N_i I_i a_{ix}$ is in the direction from the source to p_x and proportional to the voltage to the source, V_i , since $I_i \propto V_i$.

Figure 3 shows examples of the estimated magnetic field vectors by changing the voltage provided to the directional electromagnets. From Equation (2), the summation of the vector components from the positive sources (red arrows) and negative sources (blue arrows) is proportional to the magnetic field vector (green arrow) at the center of the actuator. Meanwhile, the horizontal vector component from the central electromagnet can

be neglected because there is only a vertical component at the center of the actuator. Thus, the direction of the magnetic field vector at the center can be controlled by changing the voltages to the directional electromagnets. Then, the direction of the initial magnetic force applied to the permanent magnet will follow that of the magnetic field vector.

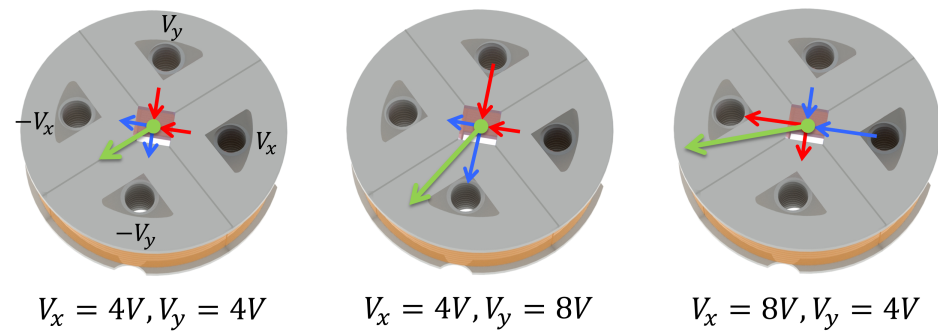


Figure 3. Examples of magnetic field vectors produced by changing the input voltages. The green, red, and blue arrows indicate the magnetic field vector at the center of the actuator and the vector components from positive and negative voltage sources. (The magnetic field vector is proportional to the sum of input voltage vectors).

The following section describes the magnetic field vector measurement setup inside the impact actuator as the input voltage to the directional electromagnet array. With the measurements, our assumption of the controllability of the magnetic field vector will be evaluated.

2.3. Distribution of the Magnetic Field inside the 2-DOF Haptic Impact Actuator

We measured the magnetic field vector inside the actuator to estimate the impact's direction from the magnetic force. Figure 4a shows the measurement setup for the magnetic field vector. A magnetometer (MLX90393, Melexis, Belgium) to measure the magnetic field vector was installed on housing that can be manually positioned on a custom-built XY stage. The central electromagnet and direction-controlling electromagnet array were located beneath and below the magnetometer, which is the same configuration as that of the impact actuator. During the measurement, the input voltage to the central solenoid was 8 V. We measured the magnetic field vector at x-positions of $\{-8, -4, 0, 4, 8\}$ mm and y-positions of $\{-8, -4, 0, 4, 8\}$ mm; in total, 25 positions. We also measured the magnetic field vector without applying the voltage to the electromagnet to cancel out the components from the outer environment, including the Earth's magnetic field. The measurement was conducted 49 times for each position, and the mean value was calculated for each location. The number of times for measurement of 49 was decided from prior measurements, where the minimum number of measurements n was calculated to be 48.4 with a confidence level of 95% [37]. We varied the voltage applied to the direction-controlling electromagnets indexed 1 and 2 in Figure 4b, which we call V_x and V_y . The range of V_x was $\{0, 3, 4, 5, 6, 7, 8\}$ V. We did not include the measurement for $V_x = 1$ and 2 V because applying the voltage values did not result in a change in the magnetic field vector from 0 V. We varied V_y for $V_x > V_y$, considering the symmetry by varying the input voltage.

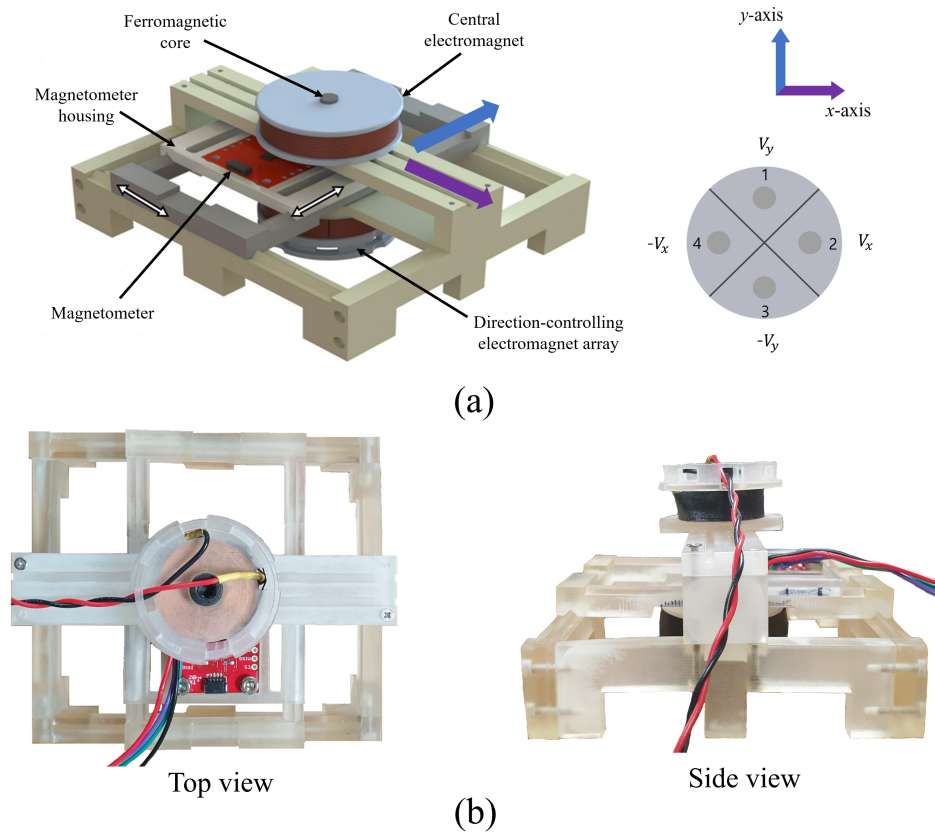


Figure 4. (a) Measurement setup of the electromagnetic field vector inside the 2-DOF haptic impact actuator. (b) Top-view of the direction-controlling electromagnet array with indices and voltage input.

2.4. Haptic Impact by Controlling the Voltage Input

To evaluate the control method for the direction of the haptic impact, we measured the acceleration as we varied the input voltage configuration. Figure 5a shows the configuration of the impact acceleration measurement setup. The impact was measured at the outer surface of the actuator to estimate the direction and magnitude of the impact. When it was measured at other positions, e.g., the center of the actuator, the acceleration was attenuated significantly, as the impact propagates from the inner wall. The impact acceleration was measured at multiple positions (angles), since measurement at a single point could not ensure the correct point of impact. A 2-DOF haptic impact actuator was attached to a measurement base with an accelerometer installed (DRV-ACC16-EVM, Texas Instruments, Dallas, TX, USA). As was the case for magnetic field measurements, the input voltage for the central electromagnet was 8 V, and the range of V_x was between 3 and 8 V with the spacing of 1 V. V_y was $\{0 \text{ V}, 3 \text{ V}, \dots, V_x\}$, i.e., $V_x \geq V_y$. Therefore, the total number of voltage combinations was $\sum_{V_y=2}^7 V_y = 27$. We rotated the measurement base by $\theta = 0, 15, 30,$ and 45 degrees; and conducted the measurements to estimate the impact angle (Figure 5b). For each voltage and rotation angle, the impact in x and y axes was measured 30 times. Then, then mean for each (V_x, V_y, θ) was calculated for a total of 108 ($27 (V_x, V_y) \times 4 \theta$) combinations. We estimated the impact angle and the acceleration for each (V_x, V_y) by taking the angle for the maximum acceleration from a B-Spline interpolation.

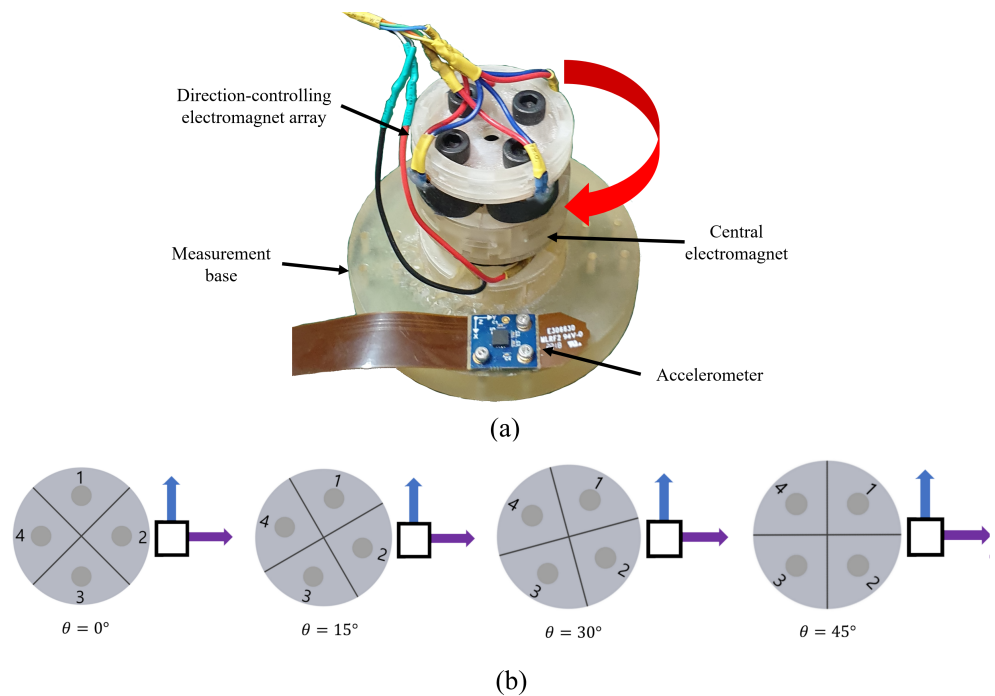


Figure 5. (a) Measure setup of the impact acceleration by controlling the voltage input. The 2-DOF haptic impact actuator was fixed on a measurement base with an accelerometer installed. The red arrow indicates the rotation of the impact actuator. (b) Top-view of the direction-controlling electromagnet array with indices and voltage input.

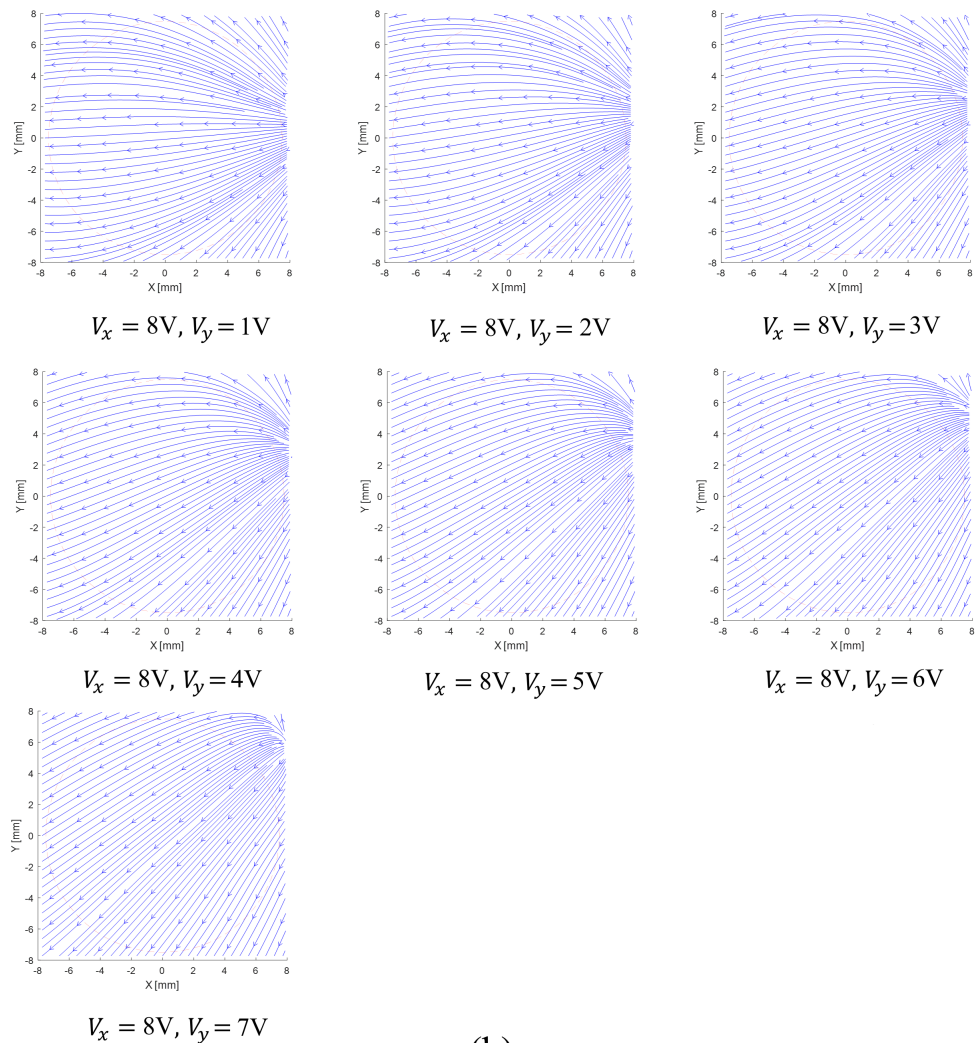
3. Results

3.1. Measurement of the Magnetic Field inside the 2-DOF Haptic Impact Actuator

The assumption of controlling the direction of the impact is that the direction of force at the center follows that of the magnetic field vector. Thus, the direction of the magnetic field vector at the center of the actuator needs to be controllable, as suggested in Equation (2). We measured the magnetic field vector at 25 positions, 49 times each, around the center of the 2-DOF impact actuator to verify the assumption. Figure 6 shows the examples of the magnetic field vector measurement. For each (V_x, V_y) , the mean of magnetic field vector at each position was recorded, as shown in the example of $(V_x = 7 \text{ V}, V_y = 8 \text{ V})$ in Figure 6a. The shaded entries in the table were used for the calculation of the mean magnetic field vector for each (V_x, V_y) . Figure 6b shows the streamlines of the magnetic field vector from the measurements for $V_x = \{1, 2, 3, 4, 5, 6, 7\} \text{ V}$ and $V_y = 8 \text{ V}$. (We plotted the streamlines of the measured vectors by using MATLAB's built-in "streamline" function, which plots interpolated 2-D or 3-D vector data). A visible trend is that an increase in V_x results in a change in streamline direction toward the x-axis.

$\bar{B}_x = -1349 \mu\text{T}$						$\bar{B}_y = -1171 \mu\text{T}$					
8	-1829.1	-1819	-1348.9	-585.39	33.962	8	-944.22	-739.03	-475.04	-62.896	258.01
4	-1791.6	-1792.7	-1385.3	-743.74	-56.523	4	-1040.2	-1002.4	-822.73	-517.4	-166.99
0	-1798.1	-1979.1	-1727.7	-1167.1	-805.15	0	-1134.7	-1361.1	-1409	-1318.7	-1261.4
-4	-1135.5	-1348.8	-1338.1	-1061.4	-725.33	-4	-789.83	-1259.8	-1565.9	-1687.4	-1605.6
-8	-651.99	-932.71	-1035.7	-1007	-643.24	-8	-530.89	-1027.3	-1406.3	-1619.2	-1526.1
$y_{\text{pos}}(\text{mm}) \backslash x_{\text{pos}}(\text{mm})$	-8	-4	0	4	8	$y_{\text{pos}}(\text{mm}) \backslash x_{\text{pos}}(\text{mm})$	-8	-4	0	4	8

(a)



(b)

Figure 6. (a) Magnetic field vector measurements in x and y axes for $V_x = 7 \text{ V}$ and $V_y = 8 \text{ V}$. (b) The streamline of magnetic field vector for $V_x = \{1, 2, 3, 4, 5, 6, 7\} \text{ V}$ and $V_y = 8 \text{ V}$.

Figure 7 shows two quiver plots. The left one is for the mean magnetic field vector measurements by (V_x, V_y) , and the right one is for the reference voltage vector formed directly by (V_x, V_y) . The average angle difference between the mean magnetic field vector and the reference voltage vector was $1.72 \pm 0.3^\circ$. Additionally, we calculated the ratio of absolute values for the measured magnetic field vector and the largest voltage vector at $V = (8, 7) \text{ V}$, denoted as $\alpha_{abs} = 168.02 \mu\text{T}/\text{V}$. We converted the voltage vector to magnetic field scale by multiplying by α_{abs} . The average difference between the mean magnetic field vector and the converted reference voltage vector was $27.97 \pm 5.13 \mu\text{T}$.

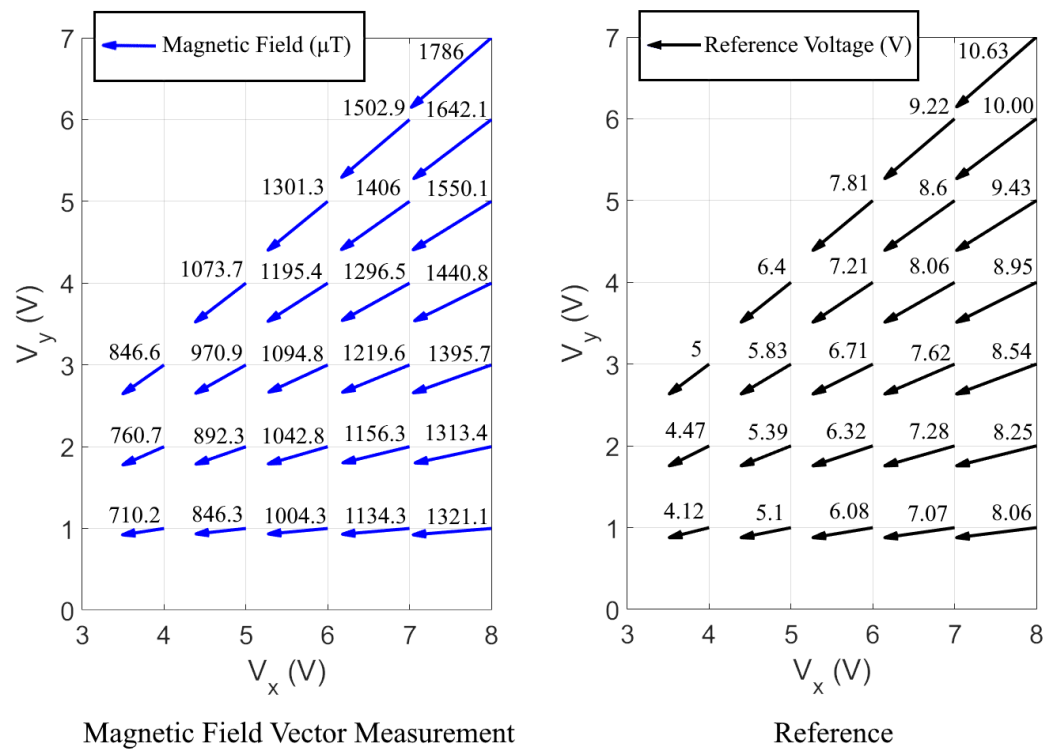


Figure 7. (Left) The quiver plot of the mean magnetic field vector by (V_x, V_y) . (Right) The quiver plot of the reference voltage vector formed by (V_x, V_y) . (The numerical value on each arrow indicates the magnitude of the vector).

Overall, the magnetic field vector measurements indicate the trend that the magnitude and the direction of magnetic field at the center follows the trend of the voltage vector. This proves that the magnetic field vector follows the trend of Equation (2).

3.2. Measurement of Haptic Impact by Controlling the Voltage Input

A 2-DOF haptic impact actuator should be able to control the direction and the magnitude of the impact. We measured the impact magnitude by rotating the haptic actuator and varying the input voltages (V_x, V_y) .

We estimated the impact angle by taking the angle where the ratio of x to y acceleration was maximum. Figure 8a shows measurement examples of x and y axes' acceleration for $\theta = 30^\circ$, $V_x = 8$ V and $V_y = 4$ V. For each (θ, V_x, V_y) , the impact was created 30 times, and the ratio of the maximum acceleration in x and y axes was calculated. Then, their mean acceleration ratio was taken. As shown in Figure 8b, the angle of impact for (V_x, V_y) , $\hat{\theta}_{x,y}$ was calculated by taking the angle of the maximum acceleration ratio. Then, the acceleration vector at (V_x, V_y) , $\hat{a}_{x,y}$ was estimated from $\hat{\theta}_{x,y}$.

Figure 9a shows the quiver plot of the acceleration vector by (V_x, V_y) . The average angle difference between the acceleration vector and the reference voltage vector (V_x, V_y) was $3.56 \pm 0.5^\circ$. Figure 9b shows the impact acceleration's absolute values plotted against (V_x, V_y) . As it was for the magnetic field vector, the ratio of the absolute value of the acceleration to that of the largest reference voltage vector ($V = (8.8)$ V), β_{abs} , was calculated. When the reference voltage vector was scaled to the acceleration, its mean difference from the measured acceleration was 1.09 ± 0.59 G.

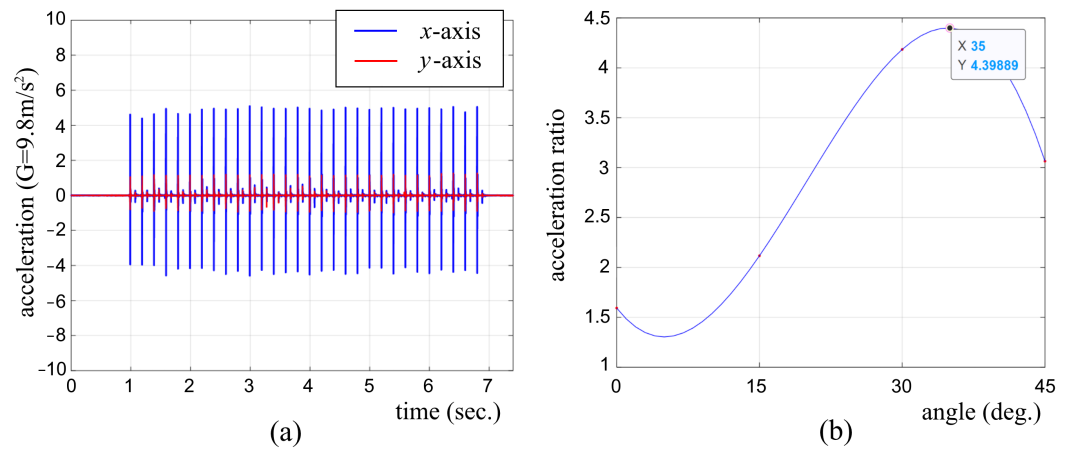


Figure 8. (a) Acceleration measurements in x and y axes for $\theta = 30^\circ$, $V_x = 8\text{ V}$, and $V_y = 4\text{ V}$. (b) Impact angle trend by θ and estimations of the impact angle.

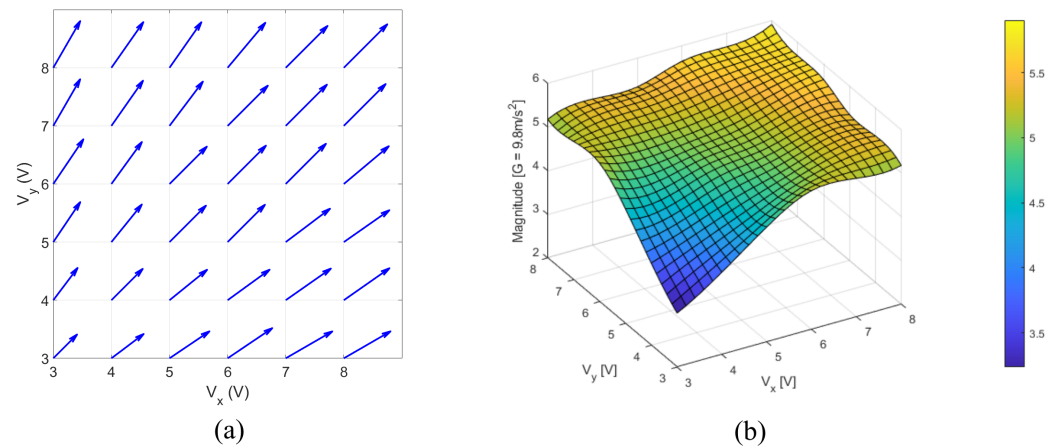


Figure 9. (a) The quiver plot of the impact acceleration vector by (V_x, V_y) . (b) The bi-cubic interpolation surface of the impact acceleration's absolute value against (V_x, V_y) .

Overall, the results of the impact acceleration measurements indicate relatively small differences in the impact angle from the reference voltage vector. In contrast, the differences in absolute values between the acceleration and the scaled reference voltage vector were significant. Thus, the desired impact I can be controlled by finding input voltages from the following process. First, the impact angle $\theta(I)$ and the magnitude of the impact $abs(I)$ are calculated. The target voltages \hat{V}_x and \hat{V}_y can be optimized by moving along the absolute acceleration surface in the direction of $\theta(I)$.

4. Discussion

In the experiments, we measured the magnetic field vectors inside the impact actuator to evaluate our assumption. The results indicate that the magnetic field vector's direction and magnitude matched those of the desired reference vector formed by the input voltages provided to the directional electromagnet array. Additionally, we measured the impacts after changing the voltage inputs to the actuator. The results indicate impact angle changed in a trend similar to the reference voltage vectors. The magnitude of an impact can be controlled by using an optimization method using the impact magnitude map obtained from the impact measurement.

A notable feature of the experimental results is that the directions of the measured magnetic field vectors followed those of the reference voltage vectors. There are studies showing that the overlap of multiple magnetic field sources can result in an overlap of magnetic field vectors [38,39]. For example, Chen et al.'s study had five electromagnets,

which resulted in overlapping of the magnetic field vectors at the sensor positions. For our case, there was a total of five magnetic field sources, one from the central electromagnet and four from the direction-controlling electromagnet array. The central electromagnet does not contribute to the horizontal component of the electromagnet vector at the center of the actuator. Thus, only the magnetic vector components from the direction-controlling electromagnet array were considered for the magnetic field vector contributing to the horizontal impact. Thus, the matching trend between the reference voltage source and the measured magnetic field vector at the center of the actuator can be explained by the overlapping of the magnetic field vector components from the direction-controlling electromagnet array.

Using the measured acceleration, the trend was that the direction of impact followed that of the reference voltage vector, though the magnitude did not. The direction of impact followed that of the reference voltage vector, which coincided with the magnetic field vector. The coincidence in direction between the impact and reference voltage vector can be explained by the fact that the attractive/repulsive force between two magnets and the magnetic force is proportional to the magnetic field [36,40]. However, the magnitude of the impact did not follow the trend of the magnitude of the reference voltage vector. Figure 9b shows that impact magnitude attenuated as the input voltage vector increased; i.e., the rate of acceleration declined as V_x and V_y increased. A possible explanation is deceleration of the permanent magnet as it passed over the direction-controlling electromagnet. An increase in the input vector means a larger attractive magnetic force toward the electromagnet. Thus, the permanent magnet would have been decelerated as it moved outward. It is also notable that a magnetic field streamline in Figure 6b passing through the center position is in a linear trend but forms a curved line. This means that a permanent magnet would have followed a slightly off-linear path until it collided with the actuator housing, contributing to the attenuation of the impact magnitude.

In future work, we will extend this study to produce a more diverse and robust haptic effect. The 2-DOF haptic impact system can be extended to a 3-DOF design which will be able to handle diverse tactile cues for a hand-held or a wearable interface. We are also considering further miniaturizing the actuator design for mobile applications. Furthermore, limitations found in the present study will be addressed in terms of mechanism and control strategy. Moreover, we plan to analyze the haptic perception of the impact created by the 2-DOF haptic impact actuator.

5. Conclusions

This study proposed a 2-DOF impact actuator for haptic applications. The actuator creates an impact by driving a permanent magnet with multiple electromagnets. A directional electromagnet array controls the direction of an impact, and a central electromagnet accelerates the impact. Regarding the direction of an impact, we assumed that changing the input voltage to the directional electromagnet array can control the direction of the magnetic field vector at the center of the actuator. The measurement results suggest that the direction and magnitude of the actuator are controllable by adjusting the input voltages supplied to the electromagnets.

The 2-DOF haptic impact actuator can be utilized for a haptic interface providing tactile feedback to a user. It can be installed inside a haptic controller to render directional haptic cues and vibration feedback. Figure 10 shows examples of the haptic impact actuators applied to a VR controller and a gamepad. The haptic impact was found to significantly benefit the realism of virtual contact compared to a typical vibrotactile actuator [41]. Thus, the augmentation of the 2-DOF haptic impact actuator is expected to increase the immersiveness of the virtual experience felt via a haptic controller. Furthermore, the 2-DOF haptic impact actuator could effectively provide directional navigational cues to the visually impaired via a cane; most can only offer a single DOF of tactile information [42]. When miniaturized, it could be used for more diverse applications, including mobile interfaces.

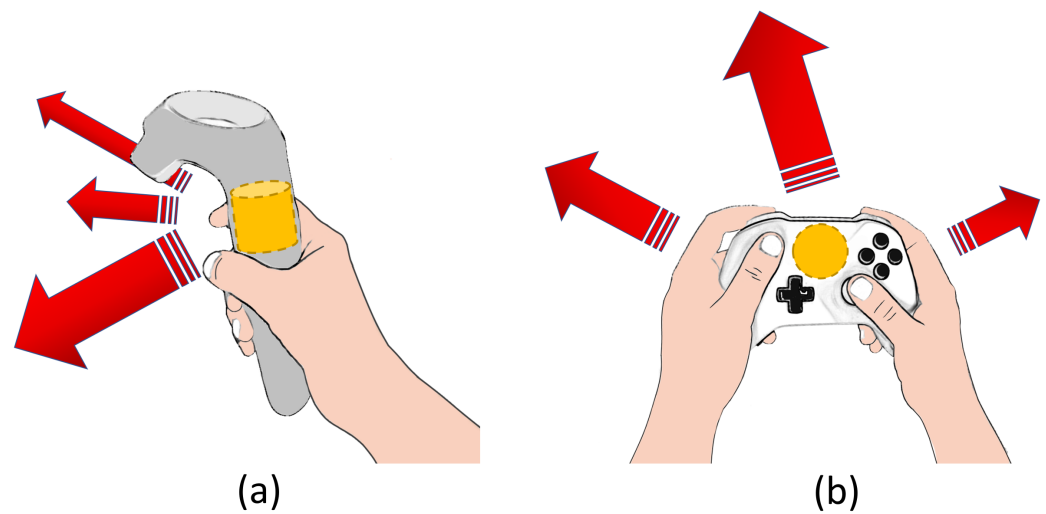


Figure 10. Application examples of the 2-DOF haptic impact actuator. (a) A VR controller with the haptic impact actuator inside. (b) A gamepad with the haptic impact actuator inside. The yellow cylinder and red arrow indicate the haptic impact actuator and the haptic impact.

6. Patents

The impact actuator prototype's overall structure and basic working principle were patented (US11075028).

Author Contributions: Conceptualization, S.K., W.L. and J.P.; methodology, S.K. and J.P.; software, S.K. and J.P.; validation, W.L. and J.P.; formal analysis, S.K., W.L. and J.P.; investigation, S.K.; resources, S.K. and J.P.; data curation, S.K. and J.P.; writing—original draft preparation, S.K., W.L. and J.P.; writing—review and editing, W.L. and J.P.; visualization, S.K. and J.P.; supervision, J.P.; project administration, J.P.; funding acquisition, J.P. All authors have read and agreed to the published version of the manuscript.

Funding: This work was supported by the National Research Foundation of Korea (NRF) Grant funded by the Korea Government (MSIT) (number NRF-2020R1A2C2014422).

Institutional Review Board Statement: Not applicable.

Informed Consent Statement: Not applicable.

Data Availability Statement: Not applicable.

Conflicts of Interest: The authors declare no conflict of interest.

Abbreviations

The following abbreviations are used in this manuscript:

DOF	Degree-of-freedom
ERM	Eccentric rotating mass
LRA	Linear resonant actuator
DEA	Dielectric elastomer actuator
VR	Virtual reality

References

- Chen, H.; Park, J.; Dai, S.; Tan, H. Design and evaluation of identifiable key-click signals for mobile devices. *IEEE Trans. Haptics* **2011**, *4*, 229–241. [[CrossRef](#)] [[PubMed](#)]
- Kim, S.-Y.; Yang, T.-H. Miniature impact actuator for haptic interaction with mobile devices. *Int. J. Control Autom. Syst.* **2014**, *12*, 1283–1288. [[CrossRef](#)]
- Yang, T.-H.; Pyo, D.; Kim, S.-Y.; Kwon, D.-S. Development and evaluation of an impact vibration actuator using an unstable mass for mobile devices. *Int. J. Control Autom. Syst.* **2016**, *14*, 827–834. [[CrossRef](#)]

4. Sekiguchi, Y.; Hirota, K.; Hirose, M. Haptic Interface using Estimation of Box Contents Metaphor. In Proceedings of the ICAT, Tokyo, Japan, 3–5 December 2003; Volume 203, pp. 3–5.
5. Liu, R.; Yang, F.; Mu, X.; Yue, H.; Zhu, C. Research on the 2-degree-of-freedom electromagnetic actuator in space. *Adv. Mech. Eng.* **2018**, *10*, 1687814017750265. [[CrossRef](#)]
6. Kim, S.; Son, B.; Lee, Y.; Choi, H.; Lee, W.; Park, J. A Two-DOF Impact Actuator for Haptic Interaction. In Proceedings of the International AsiaHaptics Conference, Incheon, Korea, 11–14 November 2018; Springer: Singapore, 2018; pp. 173–177.
7. Schorr, S.B.; Okamura, A.M. Three-dimensional skin deformation as force substitution: Wearable device design and performance during haptic exploration of virtual environments. *IEEE Trans. Haptics* **2017**, *10*, 418–430. [[CrossRef](#)] [[PubMed](#)]
8. Leonardis, D.; Solazzi, M.; Bortone, I.; Frisoli, A. A 3-RSR haptic wearable device for rendering fingertip contact forces. *IEEE Trans. Haptics* **2017**, *10*, 305–316. [[CrossRef](#)] [[PubMed](#)]
9. Chinello, F.; Pacchierotti, C.; Malvezzi, M.; Prattichizzo, D. A Three Revolute-Revolute-Spherical wearable fingertip cutaneous device for stiffness rendering. *IEEE Trans. Haptics* **2018**, *11*, 39–50. [[CrossRef](#)] [[PubMed](#)]
10. Mintchev, S.; Salerno, M.; Cherpillod, A.; Scaduto, S.; Paik, J. A portable three-degrees-of-freedom force feedback origami robot for human–robot interactions. *Nat. Mach.* **2019**, *1*, 584–593. [[CrossRef](#)]
11. Yang, T.-H.; Kim, S.-Y.; Kim, C.H.; Kwon, D.S.; Book, W.J. Development of a miniature pin-array tactile module using elastic and electromagnetic force for mobile devices. In Proceedings of the 2009 World Haptics Conference, Salt Lake City, UT, USA, 18–20 March 2009; pp. 13–17.
12. Kim, S.-Y.; An, H.-G.; Yang, T.-H. A new modular pin-array tactile device. *Int. J. Precis. Eng. Manuf.* **2015**, *16*, 1745–1751. [[CrossRef](#)]
13. Ujitoko, Y.; Taniguchi, T.; Sakurai, S.; Hirota, K. Development of Finger-Mounted High-Density Pin-Array Haptic Display. *IEEE Access* **2020**, *8*, 145107–145114. [[CrossRef](#)]
14. Sato, K.; Kajimoto, H.; Kawakami, N.; Tachi, S. Electrotactile display for integration with kinesthetic display. In Proceedings of the RO-MAN 2007—The 16th IEEE International Symposium on Robot and Human Interactive Communication, Jeju, Korea, 26–29 August 2007; pp. 3–8.
15. Kato, M.; Kono, Y.; Hirata, K.; Yoshimoto, T. Development of a haptic device using a 2-DOF linear oscillatory actuator. *IEEE Trans. Magn.* **2014**, *50*, 1–4. [[CrossRef](#)]
16. Kim G.; Hirata, K. Motion control of a two-degree-of-freedom linear resonant actuator without a mechanical spring. *Sensors* **2020**, *20*, 1954. [[CrossRef](#)] [[PubMed](#)]
17. Koo, I.M.; Jung, K.; Koo, J.C.; Nam, J.-D.; Lee, Y.K.; Choi, H.R. Development of soft-actuator-based wearable tactile display. *IEEE T-RO* **2008**, *24*, 549–558. [[CrossRef](#)]
18. Frediani, G.; Mazzei, D.; De Rossi, D.E.; Carpi, F. Wearable wireless tactile display for virtual interactions with soft bodies. *Front. Bioeng. Biotechnol.* **2014**, *2*, 31. [[CrossRef](#)] [[PubMed](#)]
19. Pyo, D.; Ryu, S.; Kyung, K.-U.; Yun, S.; Kwon, D.-S. High-pressure endurable flexible tactile actuator based on microstructured dielectric elastomer. *Appl. Phys. Lett.* **2018**, *112*, 061902. [[CrossRef](#)]
20. Ji, X. Low Voltage Fast Dielectric Elastomer Actuators. Ph.D. Thesis, The École Polytechnique Fédérale de Lausanne (EPFL), Lausanne, Switzerland, 20 September 2019.
21. Zhao, H.; Hussain, A.M.; Israr, A.; Vogt, D.M.; Duduta, M.; Clarke, D.R.; Wood, R.J. A wearable soft haptic communicator based on dielectric elastomer actuators. *Soft Robot.* **2020**, *7*, 451–461. [[CrossRef](#)]
22. Heo, Y.H.; Choi, D.-S.; Kim, D.E.; Kim, S.-Y. Flexible Vibrotactile Actuator Based on Dielectric Elastomer for Smart Handheld Devices. *Appl. Sci.* **2021**, *11*, 12020. [[CrossRef](#)]
23. Moy, G.; Wagner, C.; Fearing, R.S. A compliant tactile display for teletaction. In Proceedings of the 2000 IEEE International Conference on Robotics and Automatation (ICRA), San Francisco, CA, USA, 24–28 April 2000; pp. 3409–3415.
24. Kim, Y.; Kim, S.; Ha, T.; Oakley, I.; Woo, W.; Ryu, J. Air-jet button effects in AR. In Proceedings of the 2006 International Conference on Artificial Reality and Telexistence (ICAT), Hangzhou, China, 29 November–1 December 2006; pp. 384–391.
25. Li, M.; Luo, S.; Nanayakkara, T.; Seneviratne, L.D.; Dasgupta, P.; Althoefer, K. Multi-fingered haptic palpation using pneumatic feedback actuators. *Sens. Actuator A Phys.* **2014**, *218*, 132–141. [[CrossRef](#)]
26. He, L.; Xu, C.; Xu, D.; Brill, R. PneuHaptic: Delivering haptic cues with a pneumatic armband. In Proceedings of the 2015 ACM International Symposium on Wearable Computers (ISWC), Osaka, Japan, 7–11 September 2015; pp. 47–48.
27. Stanley, A.A.; Hata, K.; Okamura, A.M. Closed-loop shape control of a haptic jamming deformable surface. In Proceedings of the 2016 IEEE International Conference on Robotics and Automation (ICRA), Stockholm, Sweden, 16–21 May 2016; pp. 2718–2724.
28. Song, K.; Kim, S.-H.; Jin, S.; Kim, S.; Lee, S.; Kim, J.-S.; Park, J.-M.; Cha, Y. Pneumatic actuator and flexible piezoelectric sensor for soft virtual reality glove system. *Sci. Rep.* **2019**, *9*, 8988. [[CrossRef](#)]
29. Yoshida, K.T.; Nunez, C.M.; Williams, S.R.; Okamura, A.M.; Luo, M. 3-DoF Wearable, Pneumatic Haptic Device to Deliver Normal, Shear, Vibration, and Torsion Feedback. In Proceedings of the 2019 IEEE World Haptics Conference (WHC), Tokyo, Japan, 9–12 July 2019; pp. 97–102.
30. Sarkar, D.; D’Abbraccio, J.; Camboni, D.; Massari, L.; Arora, A.; Oddo, C.M. A Pneumatic Haptic Display for Collaborative Robotics Applications. In Proceedings of the 2020 IEEE International Workshop on Metrology for Industry 4.0 & IoT, Roma, Italy, 3–5 June 2020; pp. 369–373.

31. Lee, E.-H.; Kim, S.-H.; Yun, K.-S. Three-axis pneumatic haptic display for the mechanical and thermal stimulation of a human finger pad. *Actuators* **2021**, *10*, 60. [[CrossRef](#)]
32. Babic, S.I.; Akyel, C. Magnetic force calculation between thin coaxial circular coils in air. *IEEE Trans. Magn.* **2008**, *44*, 445–452. [[CrossRef](#)]
33. Ravaud, R.; Lemarquand, G.; Babic, S.; Lemarquand, V.; Akyel, C. Cylindrical magnets and coils: Fields, forces, and inductances. *IEEE Trans. Magn.* **2010**, *46*, 3585–3590. [[CrossRef](#)]
34. Avvari, P.V.; Tang, L.; Yang, Y.; Soh, C.K. Enhancement of piezoelectric energy harvesting with multi-stable nonlinear vibrations. In Proceedings of the Active and Passive Smart Structures and Integrated Systems 2013, San Diego, CA, USA, 10 April 2013; p. 86882H.
35. Schomburg, W.K.; Reinertz, O.; Sackmann, J.; Schmitz, K. Equations for the approximate calculation of forces between cuboid magnets. *J. Magn.* **2020**, *506*, 1–9. [[CrossRef](#)]
36. Cheng, D.K. *Field and Wave Electromagnetics*, 2nd ed.; Addison Wesley: Boston, MA, USA, 1989; pp. 282–294.
37. Kutz, J.N. *Data-Driven Modeling & Scientific Computation: Methods for Complex Systems & Big Data*, 1st ed.; Oxford University Press: Oxford, UK, 2013; pp. 279–286.
38. Chen, K.-Y.; Patel, S.N.; Keller, S. Finexus: Tracking precise motions of multiple fingertips using magnetic sensing. In Proceedings of the 2016 CHI Conference on Human Factors in Computing Systems, San Jose, CA, USA, 7–12 May 2016; pp. 1504–1514.
39. Chang, S.; Lin, Y.; Zheng, Y.R.; Fu, X. Simultaneous Detection of Multiple Magnetic Dipole Sources. *IEEE Trans. Magn.* **2020**, *56*, 1–11. [[CrossRef](#)]
40. Griffiths, D.J. *Introduction to Electrodynamics*, 4th ed.; Cambridge University Press: Cambridge, UK, 2017; pp. 266–288.
41. Park, C.; Park, J.; Oh, S.; Choi, S. Realistic Haptic Rendering of Collision Effects Using Multimodal Vibrotactile and Impact Feedback. In Proceedings of the 2019 IEEE World Haptics Conference (WHC), Tokyo, Japan, 9–12 July 2019; pp. 449–454.
42. Wang, Y.; Kuchenbecker, K.J. HALO: Haptic alerts for low-hanging obstacles in white cane navigation. In Proceedings of the 2012 IEEE Haptics Symposium (HAPTICS), Vancouver, BC, Canada, 4–7 March 2012; pp. 527–532.